Journal of Alloys and Compounds 583 (2014) 170–175

Contents lists available at ScienceDirect

Journal of Alloys and Compounds

journal homepage: www.elsevier.com/locate/jalcom

Structural characterizations of PtRu nanoparticles by galvanostatic pulse electrodeposition

Yu-Chi Hsieh [a], Li-Chung Chang [b], Yuan-Chieh Tseng [a,*], Pu-Wei Wu [a,*], Jyh-Fu Lee [c]

[a] Department of Materials Science and Engineering, National Chiao Tung University, Hsin-Chu 30010, Taiwan, ROC
[b] Graduate Program for Science and Technology of Accelerator Light Source National Chiao Tung University, Hsin-Chu 30010, Taiwan, ROC
[c] National Synchrotron Radiation Research Center, Hsin-Chu 30076, Taiwan, ROC

ARTICLE INFO

Article history:
Received 23 April 2013
Received in revised form 13 August 2013
Accepted 24 August 2013
Available online 5 September 2013

Keywords:
PtRu
Galvanostatic pulse electrodeposition
Electrocatalyst
Nanoparticle
EXAFS
XAS

ABSTRACT

We demonstrate that the compositions and structures of PtRu nanoparticles can be altered via adjusting plating variables during galvanostatic pulse electrodeposition. During current-on time (T_{on}), both Pt and Ru are deposited according to their respective diffusion-limiting current. However, during current-off time (T_{off}), due to difference in the redox potentials, a displacement reaction is occurring that leads to the reduction of Pt ions from the electrolyte while the Ru atoms in the PtRu nanoparticles experience oxidation reaction and corrosive dissolution simultaneously. Therefore, the duty cycle, defined as $T_{on}/(T_{on} + T_{off})$, serves as an indicator for the severity of displacement reaction that affects the PtRu makeup. Inductively-coupled mass spectrometry determines the composition as $Pt_{83}Ru_{17}$, $Pt_{64}Ru_{36}$, and $Pt_{53}Ru_{47}$ for duty cycles of 0.077, 0.111, and 0.333, respectively. Images from transmission electron microscope exhibit nanoparticles in sizes of 4–11 nm. Analysis from extended X-ray absorption fine structure (EXAFS) suggests that Pt atoms tend to segregate outward and reside at the alloy's surface upon the displacement reaction. Composition profiles from line scans of energy dispersive X-ray spectroscopy are consistent with atomic structure revealed by EXAFS.

© 2013 Elsevier B.V. All rights reserved.

1. Introduction

PtRu nanoparticles have captured great research attentions for their impressive catatlyic activities as an anode electrocatalyst for direct methanol and reformate hydrogen fuel cells [1–9]. To further enhance electrocatalytic performance, it is necessary to fabricate PtRu nanoparticles in desirable compositions or surface Pt/Ru ratios [8–17]. However, in synthesis, it is rather challenging to prepare nanoparticles with different compositions/structures from the same bath as the formulation and processing protocol need to be adjusted accordingly. Earlier, in our study of pulse deposition to form PtRu nanoparticles on carbon clothes, we observed that the resulting PtRu composition can be controlled by varying the duty cycle imposed during the plating process [18]. We realized that both Pt and Ru were electrodeposited during current-on time (T_{on}) while during current-off time (T_{off}), a displacement reaction was effective where the Pt ions were reduced from the electrolyte while the Ru atoms on the PtRu surface underwent oxidation reaction and corrosive dissolution simultaneously. Thus, the duty cycle, defined as $T_{on}/(T_{on} + T_{off})$ in a single pulse, indicates the severity of the displacement reaction that affects the resulting PtRu composition.

In literatures, the displacement reaction, also known as redox-transmetalation or spontaneous deposition, has been employed to prepare binary deposits such as CuNi, AgGe, or AuGe [19–22]. In a displacement reaction between Ru atom and Pt ions during pulse plating, during T_{off} the corrosive dissolution of Ru atom is a straightforward electrochemical step forming Ru cations in the electrolyte. An alternative route is the oxidation reaction known as cementation process where the Ru atoms become $Ru(OH)_x$ on surface and those $Ru(OH)_x$ are reduced in T_{on} of subsequent pulse. Therefore, the severity of displacement reaction and the reaction routes taken by the Ru atoms are expected to result in PtRu nanoparticles with varying compositions after multiple plating cycles. In practice, the displacement reaction can also be engaged when the PtRu nanoparticles are in contact with electrolytes containing Pt ions. For example, surface modification of commercially available PtRu nanoparticles has been demonstrated by immersing them in a concentrated hexachloroplatinic acid solution, so a Pt-enriched surface is obtained with a substantial increment in methanol electro-oxidation activities [23].

X-ray absorption spectroscopy (XAS) acquires the energy range near and above the core-level binding energy of the selected atom, which can probe chemical and physical states, sensitive to the coordination number, bonding distances surrounding around the

* Corresponding authors. Tel.: +886 3 5731898 (Y.-C. Tseng).
E-mail addresses: yctseng21@mail.nctu.edu.tw (Y.-C. Tseng), ppwu@mail.nctu.edu.tw (P.-W. Wu).

0925-8388/$ - see front matter © 2013 Elsevier B.V. All rights reserved.
http://dx.doi.org/10.1016/j.jallcom.2013.08.148

selected atom [24,25]. Previously, we have utilized XAS to investigate detailed surface PtRu arrangements by submerging Ru nanoparticles in Pt baths with various pHs, as the latter determined the type and number of ligands solvating the Pt ions [26]. In this work, we perform the characterizations of the PtRu nanoparticles derived from the galvanostatic pulse electrodeposition technique, and demonstrate that the severity of displacement reaction engenders PtRu nanoparticles with different compositions and modest segregation.

2. Experimental

PtRu nanoparticles were deposited on a carbon cloth via a galvanostatic pulse electrodeposition technique. The plating solution was prepared by mixing 99.9 wt% $RuCl_3$ (Sigma–Aldrich) and 97 wt% $NaNO_2$ (Showa) in an aqueous solution at 100 °C for 1 h, followed by dissolution of 99.9 wt% H_2PtCl_6. Subsequently, the mixture was cooled to 25 °C and 97 wt% H_2SO_4 (Showa) was added. The concentrations for the H_2PtCl_6, $RuCl_3$, $NaNO_2$, and H_2SO_4 were 0.005, 0.005, 0.050, and 0.250 M, respectively. Afterward, the mixture was aged for 2 weeks to obtain a homogeneous solution. To plate PtRu nanoparticles, rectangular pulses were imposed with fixed T_{on} (50 ms), J_a (50 mA cm^{-2}), and total coulomb charge (8 C cm^{-2}). With varying T_{off} of 100, 400, and 600 ms, the resulting samples were designated TF100, TF400, and TF600, respectively. More details about the sample preparation can be found elsewhere [18].

The exact compositions of the PtRu nanoparticles were determined by an Inductively Coupled Plasma Mass Spectrometry (ICP-MS; Agilent 7500CE). Transmission Electron Microscope (TEM; Philips Tecnai-20) was utilized to observe their morphologies and sizes. High-resolution images and atomic profiles from line scans of Energy Dispersive X-ray Spectroscopy (STEM-EDS) were obtained using a Scanning Tunneling Electron Microscope (STEM; JEOL ARM200F). XAS measurements over Pt L_{III}-edge (11,564 eV) and Ru K-edge (22,117 eV) were performed at beam lines of BL01C1 and BL17C1, respectively at Taiwan Light Source, National Synchrotron Radiation Research Center (NSRRC), Hsinchu, Taiwan. The measurements were carried out in a fluorescence detection mode at room temperature. A Pt foil, H_2PtCl_6 electrolyte, as well as Ru and RuO_2 powders were served as references for Pt L_{III}-edge and Ru K-edge XAS spectra.

Extended X-ray absorption fine structure (EXAFS) and X-ray absorption near edge structure (XANES) data analysis and fitting were processed by an IFEFFIT 1.2.11c data analysis package (Athena, Artemis, and FEFF6). The recorded profiles were calibrated by aligning against the reference in each scan. During measurements, multiple spectra for a single absorption edge were collected and averaged to achieve better signal quality. Each raw spectrum was pre-edge subtracted to remove the background and then was normalized with respect to the edge jump. The normalized spectrum was converted into k-space and was k-weighted properly, and finally was Fourier transformed (FT) into r-space. Specific ranges in k-space for the Fourier transformation were selected from 3.32 to 12.74 $Å^{-1}$ for the Pt L_{III}-edge and from 4.01 to 13.42 $Å^{-1}$ for the Ru K-edge. The ranges of r-space for the curve fitting were established without phase correction from 1.90 to 3.17 Å for Pt and from 1.70 to 2.73 Å for Ru. Relevant structural characteristics were fitted by Artemis with theoretical standards generated by FEFF6 code. The fitting parameters include coordination number (N), bond distance (R), Debye–Waller factor $\left(\Delta\sigma_j^2\right)$, and inner potential shift (ΔE_0). Analysis details have been published previously [26].

3. Results and discussion

Fig. 1 demonstrates the TEM images for samples of TF100, TF400, and TF600, respectively. The size distribution for the PtRu nanoparticles appeared relatively broad as their average values were estimated to be 7.4 ± 3.9, 5.1 ± 2.6, and 12.7 ± 5.6 nm, respectively. A wider size distribution was anticipated since in pulse electrodeposition, every single pulse engendered independent events of nucleation and growth simultaneously. Table 1 presents the composition variation for the PtRu nanoparticles and their respective coulomb efficiency in electrodeposition. As listed, the coulomb efficiency was rather subdued at 1.83–3.83% because most of the currents were not responsible for the formation of PtRu nanoparticles during T_{on}. Instead, the majority of coulomb charge was consumed in parasitic reactions including proton reduction, water electrolysis, and reduction of surface oxides and oxyhydroxides formed during T_{off}. In addition, we would like to point out that the contribution of capacitive current was negligible in our work as the T_{on} and T_{off} are considerably longer than the typical T_{on} and T_{off} of 1 ms where the capacitive current becomes a tangible factor [18].

Table 1
Pt/Ru atomic ratios for the TF 100, TF400 and TF600 PtRu nanoparticles, and the corresponding electrodeposition coulomb efficiencies for the three samples.

	Duty cycle[a]	Coulomb efficiency (%)	Pt/Ru Atomic ratio[b]
TF100	0.333	2.58	53/47
TF400	0.111	1.83	64/36
TF600	0.077	2.83	83/17

[a] Duty cycle is defined as $T_{on}/(T_{on} + T_{off})$, and T_{on} = 50 ms, T_{off} = 100, 400, and 600 ms, respectively.
[b] From ICP-MS.

Composition analysis from ICP-MS indicated $Pt_{53}Ru_{47}$, $Pt_{64}Ru_{36}$, and $Pt_{83}Ru_{17}$ for TF100, TF400, and TF600, respectively. It is noteworthy that these values represent the average PtRu makeup since the ICP-MS dissolves the entire sample in atomic states. In principle, a displacement reaction between Ru atoms in the PtRu nanoparticles and Pt ions in the electrolyte during T_{off} allowed the deposition of excess Pt atoms on the PtRu surface, so the average composition was expected to move toward a Pt-rich one. This behavior was consistent with our finding where a smaller duty cycle produced $Pt_{83}Ru_{17}$ while a larger duty cycle rendered $Pt_{53}Ru_{47}$ instead. To further determine relative locations of Pt and Ru atoms within our samples, we carried out composition analysis using STEM-EDS on individual PtRu nanoparticles, and the resulting line scan profiles for TF100, TF400, and TF600 are displayed in Fig. 2. As shown, their respective widths were 7.12, 6.21, and 16.2 nm, and the relative atomic percentages (vertical axis) of Pt (black) and Ru (red) are plotted with respect to the probed position (horizontal axis). The line scans suggested that our samples displayed a homogeneous state, and the atomic percentages are consistent with results from ICP-MS.

X-ray absorption spectroscopy (XAS) was conducted to explore the element-specific local structures of Pt and Ru for the three investigated samples, by probing Pt L_{III} and Ru K edges. Fig. 3(a)

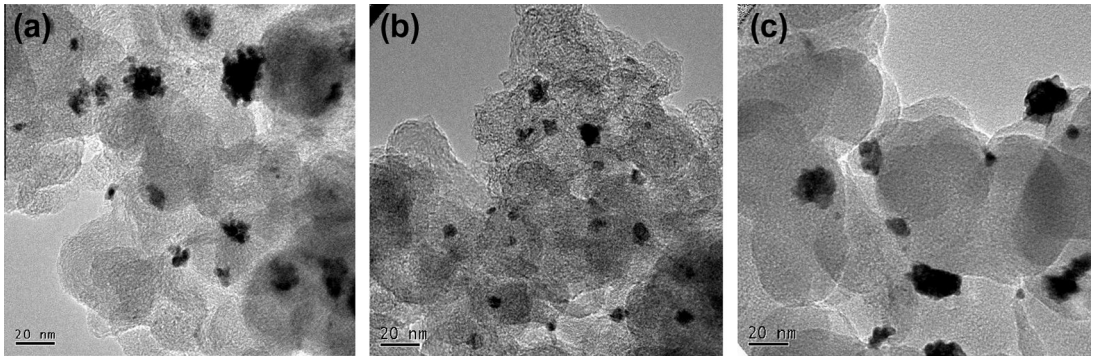

Fig. 1. The TEM images for (a) TF100, (b) TF400, and (c) TF600 PtRu nanoparticles.

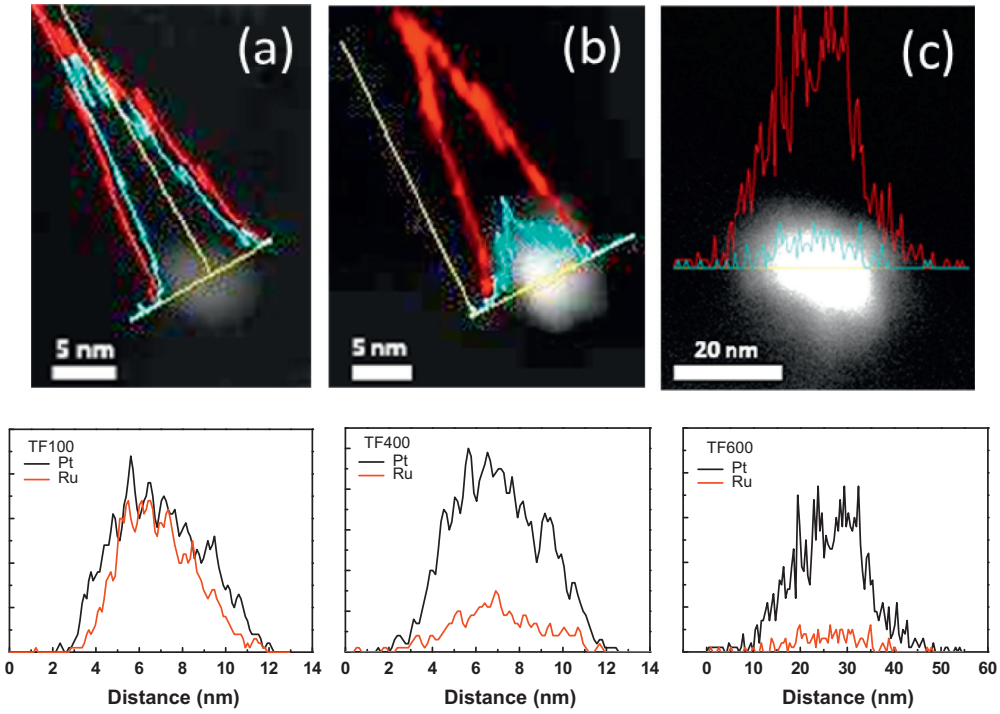

Fig. 2. STEM EDS line spectra for (a) TF100, (b) TF400, and (c) TF600 PtRu nanoparticles. In the bottom are the re-plotted spectra corresponding to the upper spectra, where Pt and Ru compositional distributions are presented by black and red colors, respectively. (For interpretation of the references to colour in this figure legend, the reader is referred to the web version of this article.)

demonstrates TF-dependent Pt L_{III}-edge XANES and EXAFS spectra. The XANES corresponded to the Pt 2p → 5d photo-excitation process with the white-line intensity reflecting the available vacancy in the 5d orbital, as well as the binding energy of the 2p core electrons as highlighted by the inset figure. The binding energy of Pt has been reported to decrease while alloying with Ru [27]. This is because a Ru–Pt bond contributed a binding energy different than a Pt–Pt bond with respect to Pt, which can be reflected by the white-line intensity. On the contrary, in Fig. 3(b) the TF-dependency was imperceptible in Ru XANES, due to the intrinsically weak white-line intensity of the *K*-edge that corresponded to 1s → 4p photo-excitation. However, in the extended energy range the Ru spectra of the investigated samples were less oscillatory than that of the reference Ru. This is expected to give rise to a disordered atomic environment around the Ru that would smear the local ordering of the Ru–Pt bond.

Fig. 4(a and b) present *k*-space EXAFS for the Pt L_{III} and Ru *K* edge, respectively, together with the reference Pt and Ru. In Fig. 4(a) the reference Pt featured a superposition of two frequencies/wavelengths particularly around 9 and 10 $Å^{-1}$, meaning that it is necessary to take into account more than the nearest-neighbor shell. In contrast, such phenomenon became obscure in the investigated samples, which mainly featured one dominant frequency contributed from the nearest-neighbor shell, due to reduced coordination number and a smaller Debye–Waller factor in the nanoparticle structure. These two factors also accounted for the discrepancy in spectral amplitude. Nevertheless, the phase of oscillation and spectral amplitude appeared to approach to those of the Pt reference with increasing T_{off}. The frequency and wavelength of TF600 were in a close proximity to those of the reference Pt, implying that in this particular sample the metallic nature of Pt was more dominant in comparison with TF100 and TF400. This is consistent with the ICP-MS results (Table 1) where the highest Pt/Ru ratio was obtained in TF600. In Fig. 4(b), the EXAFS amplitudes of all the Ru were largely suppressed as a result of the less oscillatory

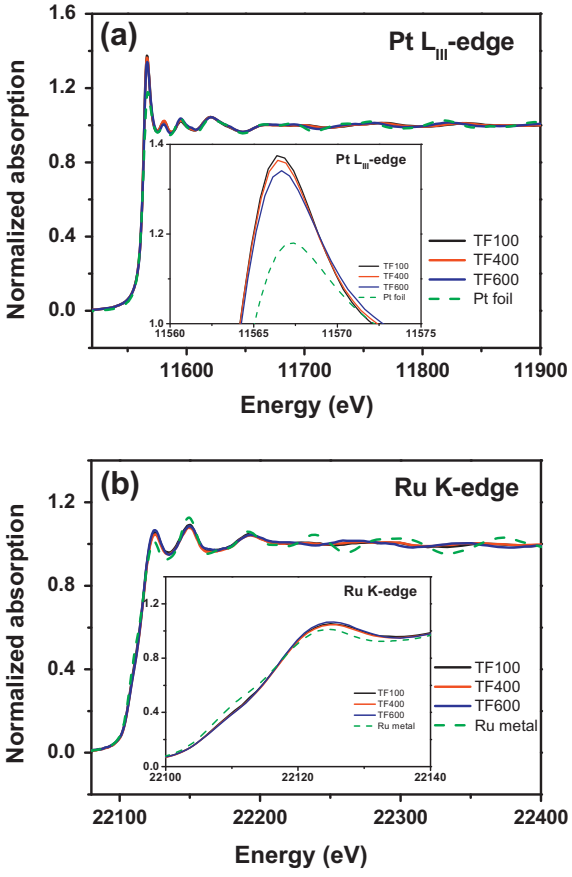

Fig. 3. The XAS spectra for (a) Pt L_{III}-edge and (b) Ru *K*-edge, of TF100, TF400, TF600 samples, in comparison with reference Pt foil and Ru metal.

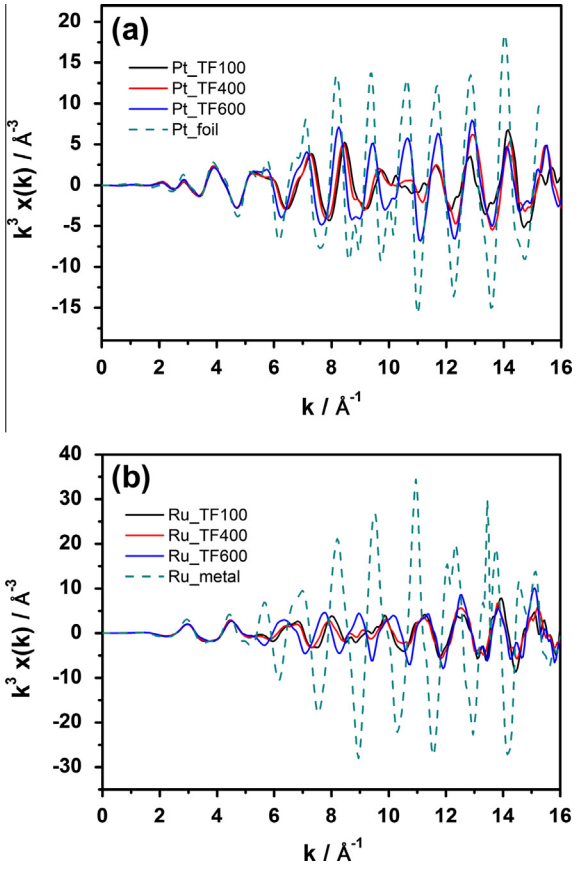

Fig. 4. The *k*-space EXAFS spectra for (a) Pt L_{III}-edge and (b) Ru *K*-edge, of TF100, TF400, TF600 samples, in comparison with reference Pt foil and Ru metal.

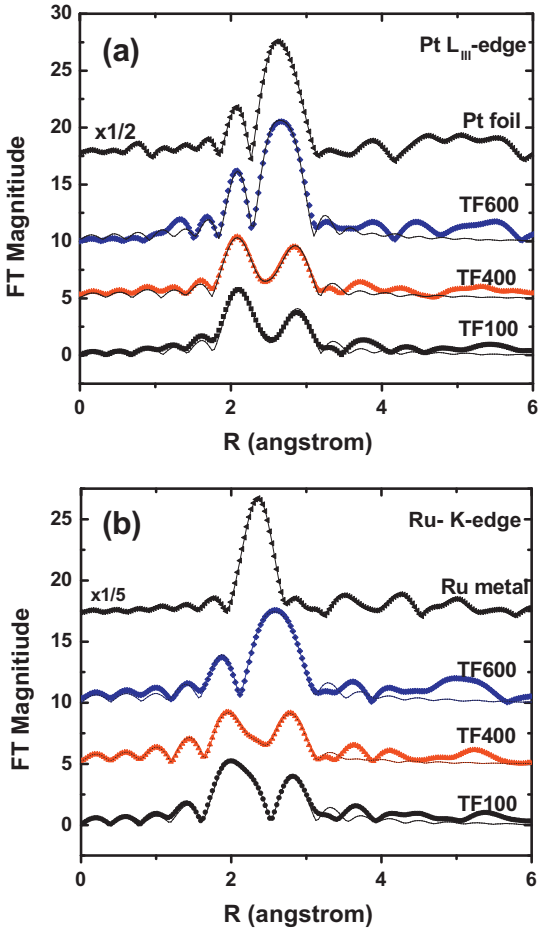

Fig. 5. The Fourier-transformed EXAFS Spectra for (a) Pt L_{III}-edge and (b) Ru *K*-edge, of TF100, TF400, TF600 samples, in comparison with reference Pt foil and Ru metal.

natures in the extended energy range of *E*-space EXAFS (Fig. 3(b)). It came to our attention that all the phase shifts of Ru EXAFS were towards a lower *k* range in comparison with the reference Ru, likely due to the formation of Pt–Ru bonds with a longer bond-distance than Ru–Ru [28–31].

We Fourier transformed (FT) the k^3 weighted $\chi(k)$ data into *r*-space, as provided in Fig. 5(a and b) for Pt and Ru, respectively, to place a more quantitative footing for the Pt (Ru) local structures. In FT-EXAFS, the resulting peaks corresponded to the position of successive shells of the centered Pt (Ru). In Fig. 5(a), the Pt FT-EXAFS of TF600 was nearly identical to that of the reference Pt, indicative of a major phase of metallic Pt. Despite that the 1st atomic shells of TF100 and TF400 were correctly positioned, the shells were rather smeared and overlapped with the 2nd shells. This suggested that considerable fraction of the Pt–Ru bonds have smeared the FT-EXAFS generated by the Pt–Pt bonds. Interestingly, in Fig. 5(b) the Ru FT-EXAFS of the investigated samples were fundamentally different than that of the reference Ru, but rather similar to that of the Pt, especially TF600. Obviously a picture where Pt dominated the PtRu's structural properties was preserved microscopically, with Pt-domination increased upon displacement reaction.

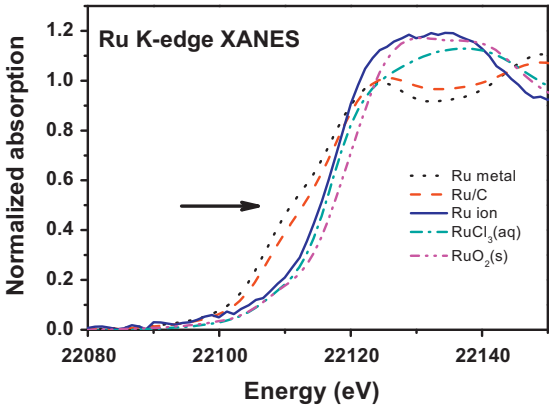

Fig. 6. The Ru *K*-edge XANES spectra of Ru ions after displacement reaction (marked as Ru ion, blue color), along with reference Ru metal, Ru/C, $RuCl_3$(aq) and RuO_2(s). (For interpretation of the references to colour in this figure legend, the reader is referred to the web version of this article.)

Table 2
EXAFS fitting parameters gained from Pt L_{III}-edge and Ru *K*-edge for TF100, TF400 and TF600 PtRu nanoparticles. Details about the notations are described in content.

	N_{Pt-Ru}	N_{Pt-Pt}	ΣN_{Pt}	N_{Ru-Pt}	N_{Ru-Ru}	ΣN_{Ru}	P_{Pt}	P_{Ru}	Pt (at.%)	Ru (at.%)
TF100	4.16	5.91	10.07	4.69	3.54	8.23	0.41	0.57	51.9	48.1
TF400	2.25	5.9	8.15	6.2	2.98	9.18	0.28	0.68	65.5	34.5
TF600	1.0	8.98	9.98	9.01	1.52	10.53	0.1	0.85	83.4	16.6

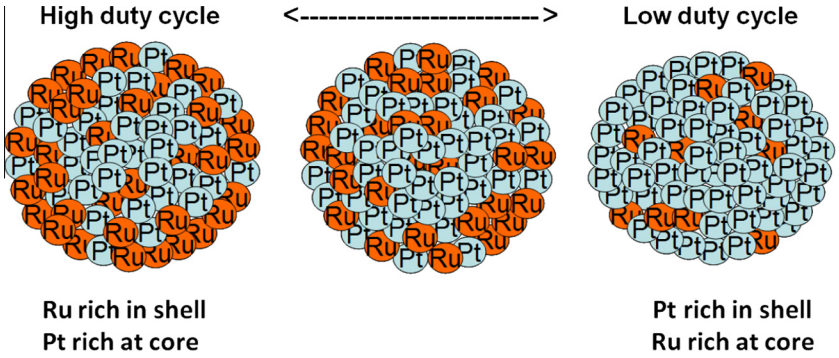

Fig. 7. Schematic illustrations for the structural evolution of PtRu nanoparticles with displacement reaction, showing samples of TF100 (left, high duty cycle), TF400 (middle, medium duty cycle), and TF600 (right, low duty cycle).

The FT-EXAFS spectra were subsequently fitted by IFEFFIT Artemis program to analyze the coordination number of the selected atoms, using fixed Pt–Ru (R_{Pt-Ru} = 2.65 A) and Pt–Pt (R_{Pt-Pt} = 2.70 A) bond distances. The fitting results were summarized in Table 2. Here, N_{Pt} referred to the total coordination number of the centered Pt, but N_{Pt-Ru} represented the coordination number of the Pt only surrounded by the Ru, and the same principle was applied to all notations. Furthermore, a term of P_{Pt} (P_{Ru}) was created to estimate the possibility for the centered Pt (Ru) encountering a *different* neighboring atom of Ru (Pt), which can be mathematically expressed as the following relations, according to Refs. [30–32].

$$P_{Pt} = \frac{N_{Pt-Ru}}{\Sigma N_{Pt}}; \quad P_{Ru} = \frac{N_{Ru-Pt}}{\Sigma N_{Ru}}$$

The reciprocal of P_{Pt} (P_{Ru}) revealed the tendency for assembling the same atomic species in statistics. By summarizing the fitting results in Table 2, we observe opposite trends for Pt and Ru deposition with increasing T_{off}, where Pt continuously deposited onto the surface whereas Ru was removed. This provided a conclusive perspective to the structural evolution of the displacement reaction in addition to the analyses above. To acquire the chemical state of the removed Ru, an XANES comparison for the Ru of displacement reaction (DR), Ru on a carbon substrate (Ru/C), Ru of $RuCl_3$ and of RuO_2, is presented in Fig. 6. The spectral shape of the Ru in DR was close to those of $RuCl_3$ and RuO_2. Since the absorption rising energy of the Ru in DR was almost overlapped with that of $RuCl_3$, it is reasonable to assign +3 state to the removed Ru ions for the displacement reaction.

As the displacement reaction can be characterized by a Pt-on, Ru-off mechanism, tracking structural evolution upon the reaction was of great interest especially concerning the PtRu's technological application. For EXAFS, it was collected by a transmission mode with an X-ray fully penetrating the PtRu, so the probed coordination number ΣN can reveal whether the selected atom segregates outward (lower ΣN) or stays at the core (higher ΣN) of the alloy. We noticed that ΣN_{Pt} was larger than ΣN_{Ru} in TF100 while became smaller than ΣN_{Ru} in TF600, which indicated a tendency of segregating outward for the Pt upon displacement reaction. By summarizing the results from EXAFS, STEM-EDS and ICP-MS, a picture can be illustrated where TF 600 featured a modest segregation of Pt at surface, but TF100 was rather a homogeneous PtRu solid solution. A scheme illustrating the structural evolution with the displacement reaction is therefore depicted in Fig. 7.

4. Conclusion

Galvanostatic pulse electrodeposition was employed to fabricate PtRu nanoparticles on carbon clothes. With fixed T_{on} and coulomb charge, we varied the T_{off} and the severity of displacement reaction was altered accordingly. Results from ICP-MS determined that with a smaller duty cycle, a severe displacement reaction occurring during T_{off} allowed excess Pt deposition from the electrolyte to form $Pt_{83}Ru_{17}$ (TF600) nanoparticles, while with a larger duty cycle the composition became $Pt_{53}Ru_{47}$ (TF100) instead. XANES and EXAFS analyses revealed structural evolution upon displacement reaction and indicated a modest segregation of Pt at surface for TF600. Equipment assistances from Professor George Tu and Professor Pang Lin are greatly appreciated. Financial support from the National Science Council of Taiwan (98-2221-E-009-040-MY2; 98-2112-M-009-022-MY3) is acknowledged.

References

[1] K.R. Lee, M.K. Jeon, S.I. Woo, Appl. Catal., B 91 (2009) 428–433.
[2] F.H.B. Lima, E.R. Gonzalez, Appl. Catal., B 79 (2008) 341–346.
[3] S.H. Oh, R.M. Sinkevitch, J. Catal. 142 (1993) 254–262.
[4] S. Alayoglu, A.U. Nilekar, M. Mavrikakis, B. Eichhorn, Nat. Mater. 7 (2008) 333–338.
[5] C.T. Hsieh, Y.W. Chou, W.Y. Chen, J. Alloys Comp. 466 (2008) 233–240.
[6] J.M. Sieben, M.M.E. Duarte, C.E. Mayer, J. Alloys Comp. 509 (2011) 4002–4009.
[7] Y.J. Song, S.-B. Han, J.M. Lee, K.W. Park, J. Alloys Comp. 473 (2009) 516–520.
[8] Y.C. Wei, C.W. Liu, W.J. Chang, K.W. Wang, J. Alloys Comp. 509 (2011) 535–541.
[9] Y. Liang, J. Li, Q.C. Xu, R.Z. Hu, J.D. Lin, D.W. Liao, J. Alloys Comp. 465 (2008) 296–304.
[10] K.Y. Chan, J. Ding, J. Ren, S. Cheng, K.Y. Tsang, J. Mater. Chem. 14 (2004) 505–516.
[11] C. Yang, X. Hu, D. Wang, C. Dai, L. Zhang, H. Jin, S. Agathopoulos, J. Power Sources 160 (2006) 187–193.
[12] A.N. Gavrilov, E.R. Savinova, P.A. Simonov, V.I. Zaikovskii, S.V. Cherepanova, G.A. Tsirlina, V.N. Parmon, Phys. Chem. Chem. Phys. 9 (2007) 5476–5489.
[13] D. Chu, S. Gilman, J. Electrochem. Soc. 143 (1996) 1685–1690.
[14] A.S. Aricò, P.L. Antonucci, E. Modica, V. Baglio, H. Kim, V. Antonucci, Electrochim. Acta 47 (2002) 3723–3732.
[15] H.A. Gasteiger, N. Marković, P.N. Ross Jr, E.J. Cairns, Electrochim. Acta 39 (1994) 1825–1832.
[16] H.A. Gasteiger, N. Markovic, P.N. Ross, E.J. Cairns, J. Phys. Chem. 97 (1993) 12020–12029.
[17] F. Maillard, F. Gloaguen, J.M. Leger, J. Appl. Electrochem. 33 (2003) 1–8.
[18] Y.-C. Hsieh, P.-W. Wu, Y.-J. Lu, Y.-M. Chang, J. Electrochem. Soc. 156 (2009) B735–B742.
[19] S. Roy, D. Landolt, J. Electrochem. Soc. 142 (1995) 3021–3027.
[20] S. Roy, M. Matlosz, D. Landolt, J. Electrochem. Soc. 141 (1994) 1509–1517.
[21] Q. Zhu, C.L. Hussey, J. Electrochem. Soc. 148 (2001) C395–C402.
[22] L.A. Porter, H.C. Choi, A.E. Ribbe, J.M. Buriak, Nano Lett. 2 (2002) 1067–1071.
[23] C.W. Kuo, I.T. Lu, L.C. Chang, Y.C. Hsieh, Y.C. Tseng, P.W. Wu, J.F. Lee, Surface modification of commercial PtRu nanoparticles for methanol electro-oxidation, J. Power Sources (2013), http://dx.doi.org/10.1016/j.jpowsour.2013.04.001.
[24] C.H. Chen, L.S. Sarma, D.Y. Wang, F.J. Lai, C.C. Al Andra, S.H. Chang, D.G. Liu, C.C. Chen, J.F. Lee, B.J. Hwang, ChemCatChem 2 (2010) 159–166.
[25] B.-J. Hwang, L.S. Sarma, C.-H. Chen, C. Bock, F.-J. Lai, S.-H. Chang, S.-C. Yen, D.-G. Liu, H.-S. Sheu, J.-F. Lee, J. Phys. Chem. C 112 (2008) 19922–19929.
[26] Y.C. Hsieh, L.C. Chang, P.W. Wu, Y.M. Chang, J.F. Lee, Appl. Catal. B 103 (2011) 116–127.
[27] A. Lewera, W.P. Zhou, R. Hunger, W. Jaegermann, A. Wieckowski, S. Yockel, P.S. Bagus, Chem. Phys. Lett. 447 (2007) 39–43.
[28] M.S. Nashner, A.I. Frenkel, D. Somerville, C.W. Hills, J.R. Shapley, R.G. Nuzzo, J. Am. Chem. Soc. 120 (1998) 8093–8101.

[29] S. Alayoglu, P. Zavalij, B. Eichhorn, Q. Wang, A.I. Frenkel, P. Chupas, ACS Nano 3 (2009) 3127–3137.
[30] H. Nitani, T. Nakagawa, H. Daimon, Y. Kurobe, T. Ono, Y. Honda, A. Koizumi, S. Seino, T.A. Yamamoto, Appl. Catal. A 326 (2007) 194–201.
[31] B.J. Hwang, L.S. Sarma, C.H. Chen, C. Bock, F.J. Lai, S.H. Chang, S.C. Yen, D.G. Liu, H.S. Sheu, J.F. Lee, J. Phys. Chem. C 112 (2008) 19922–19929.
[32] B.J. Hwang, L.S. Sarma, J.M. Chen, C.H. Chen, S.C. Shih, G.R. Wang, D.G. Liu, J.F. Lee, M.T. Tang, J. Am. Chem. Soc. 127 (2005) 11140–11145.